



# DFT studies on structure, electronics, bonding nature, NBO analysis, thermodynamic properties, molecular docking, and MM-GBSA evaluation of 4-methyl-3-[2-(4-nitrophenyl)-1,3-dioxo-2,3-dihydro-1*H*-isoindole-5-amido]benzoic acid: a potent inhibitor of Graves' disease

Emmanuel Israel Edache<sup>1,2</sup> · Adamu Uzairu<sup>2</sup> · Paul Andrew Mamza<sup>2</sup> · Gideon Adamu Shallangwa<sup>2</sup> · Muhammad Tukur Ibrahim<sup>2</sup>

Received: 16 November 2023 / Accepted: 3 February 2024  
© The Author(s) 2024

## Abstract

A calculation analysis on the molecular structure and energy of 4-methyl-3-[2-(4-nitrophenyl)-1,3-dioxo-2,3-dihydro-1*H*-isoindole-5-amido]benzoic acid (COD30) is carried out with the 6-311G (d,p) basis set by the DFT/RB3LYP method as an anti-graves' disease treatment. The calculated FT-IR spectrum is strongly correlated with the vibrational spectra reported in the literature. To evaluate the entire electron density and organic reactive sites of COD30, molecular electrostatic potential (MEP) and frontier molecular orbitals (FMO) were analyzed. The density of states analysis is used to determine the orbital molecular contributions (DOS and PDOS). In comparison to methimazole (MMI) and propylthiouracil, COD30 showed more encouraging docking results, and it also offered golden binding contacts in addition to an improvement in docking energy (PTU). The outcomes of bioactivity prediction and MD simulation indicate that COD30 could be further developed into an inhibitor of Graves' disease.

**Keywords** DFT · NBO · Docking · Molecular dynamic simulations · MM/GBSA · Graves' disease

## 1 Introduction

Graves' disease (originally known as exophthalmic goiter) is an autoimmune disease that results in generalized over-activity of the entire thyroid gland [1, 2]. By detecting and eliminating bacteria, viruses, and other potentially harmful foreign substances, the immune system typically guards the body against infection [3]. However, in autoimmune diseases, the body's cells and organs are attacked by the immune system [4]. The most frequent cause of hyperthyroidism, Graves' disease, also known as toxic diffuse goiter, accounts for 60% to 80% of cases of the condition worldwide [5]. When the thyroid yields more thyroid

hormone than the body requires, a condition known as hyperthyroidism results [6]. Thyroid-stimulating immunoglobulin (TSI), also known as a TSH receptor antibody, is an antibody that the immune system creates in Graves' disease that binds to thyroid cells [6, 7]. Because TSI mimics TSH, it causes the thyroid to overproduce thyroid hormone [7]. Sometimes the TSI antibody inhibits the production of thyroid hormone, leading to conflicting symptoms that can make a diagnosis challenging [8]. Graves' disease patients may experience typical signs of an overactive thyroid, such as anxiety or irritability, fatigue or muscle weakness, intolerance to heat, difficulty sleeping, hand tremors, a fast and irregular heartbeat, frequent bowel movements or diarrhea, weight loss, and an enlarged thyroid gland that causes a swollen throat and impairs normal breathing and swallowing [8, 9]. A few graves disease sufferers also have thickening and redness of the skin on their shins [10]. Additionally, individuals with Graves' disease may have the appearance of having enlarged eyes due to the retraction of their eyelids into their orbits and the protrusion of their eyes from those orbits [4]. The research reveals that it

✉ Emmanuel Israel Edache  
edacheson2004@gmail.com

<sup>1</sup> Department of Pure and Applied Chemistry, University of Maiduguri, Maiduguri, Borno, Nigeria

<sup>2</sup> Department of Chemistry, Faculty of Physical Science, Ahmadu Bello University, P.M.B 1045, Zaria, Kaduna, Nigeria

is impossible to predict who may develop Graves' disease [11]. However, likely, factors like age, gender, heredity, emotional stress, and chronic stress are all contributing factors [12]. Graves' disease typically affects individuals who are under the age of 40, and women are seven to eight times more likely than men to develop it [13]. Women between the ages of 30 and 60 are most frequently affected. Additionally, having a family history of the disease increases the risk of developing Graves' disease [12, 14]. Researchers were unable to identify a particular gene that causes the disease to be passed from parent to child. It is challenging to predict who will be affected, although some people inherit an immune system that can produce antibodies against healthy cells [15, 16]. Graves' disease is more likely to develop in those who have other autoimmune diseases and those taking highly active antiretroviral therapy (HAART) for immune reconstitution [17]. Type 1 diabetes, rheumatoid arthritis, and vitiligo, a condition in which some areas of the skin are unpigmented, are diseases connected to Graves' disease [18, 19].

Today, it is evident that some genes contribute to the genetic predisposition to Graves' disease. One of the genes that predispose to Graves' disease that has received the most research is the human leukocyte antigen (HLA) gene [20]. This gene's mutations have been connected to the illness in numerous ways. Numerous autoimmune diseases, such as Graves' disease, have been linked to lymphoid tyrosine phosphatase, which is encoded by the gene protein tyrosine phosphatase non-receptor type 22 (PTPN22). Thyrotropin receptor (TSHR), thyroglobulin gene, FCRL3, SCGB3A2, and CTLA4 are additional genes linked to GD risk [21].

Due to the need for high precision when estimating (relative) binding affinities, quantum mechanical (QM) approaches are growing in popularity in computational drug design and research [22]. Particularly when compared to other ab initio methodologies now in use, density functional theory (DFT) computations offer excellent levels of accuracy with comparable computation times and are less expensive in terms of computational resources [23]. Herein, we are using the Quantum chemical calculations with the help of DFT to predict the optimized molecular structure and vibrational studies of 4-Methyl-3-[2-(4-nitrophenyl)-1,3-dioxo-2,3-dihydro-1*H*-isoindole-5-amido]Benzoic acid, abbreviated as (COD30). Because the investigated molecule has a broad variety of pharmacological action, including the ability to treat autoimmune disorders, its comparable molecular structures make it an important synthetic class in drug design [5, 24]. The calculation of the potential energy distribution (PED) served as the foundation for the vibrational investigations. Analysis using the Frontier Molecular Orbital (FMO) was carried out. Furthermore, it has been suggested that the Fukui functional analysis will determine the relationships between the structure and activity of a

molecule. The molecular electrostatic potential (MEP) surface was analyzed.

In recent years, the search for new medications to treat a range of infections has made substantial use of computational techniques including molecular docking and molecular dynamics simulations [24, 25]. Molecular docking studies were used to examine a drug's propensity for binding to various receptors in the case of Graves' disease. In silico molecular docking research was done to investigate the anti-graves' disease properties of the CPD30 molecule on protein tyrosine phosphatase non-receptor type 22 (PTPN22), thyroid hormone receptor alpha1 gene (THRA1), and thyroid hormone receptor beta (ERBA2). Thanks to this, the chemical's binding conformation and affinities could then be identified. The kinetics of the complex formed between the drug and its targets was also studied using molecular dynamics simulations. By employing the Molecular mechanics with generalized Born and surface area solvation (MM/GBSA) binding free energy approach, the results of the docking and molecular dynamic simulations were further validated. Overall, these computational tools have helped identify potential therapeutic drugs for treating various infections.

## 2 Materials and methods

The software database GaussView v6.0.16 [26] provided the initial atomic coordinates for the geometry optimization. The ground-state molecular structures of the reference medications (methimazole and propylthiouracil) and COD30 were optimized using DFT (RB3LYP) methods at the 6-311G (d,p) basis set level, and the vibrational frequency calculations were performed using this optimized structure. All calculations (vibrational wave numbers, geometric parameters, and other molecular properties) were carried out on a computer system using the molecular visualization software GaussView and the software package Gaussian 09 [26]. Additionally, the calculated vibrational frequencies are made clearer by using the VEDA 4 program to examine the potential energy distribution (PED) of all fundamental vibrational modes [27]. Finally, based on the optimized structures, some physical and chemical (thermochemistry) properties were calculated.

### 2.1 Protein and docking simulations

Targeted Graves' disease crystal structures in three dimensions (PDB IDs: 4J51, 1NAV, and 1NAX) were gathered from the protein database in PDB format. Using client software packages from Discovery Studio, all heteroatoms (i.e., co-crystallized structure, chains B and C, water molecules) were eliminated from the crystal structures. The MGL software package's AutoDockTools (ADT) v1.5.7 [28] was used

to modify the proteins' pdb chain A format into a pdbqt format by adding polar hydrogen and Gasteiger charges. The prepared proteins were used to conduct a docking simulation on the improved drugs. The software AMDock v1.5.2 [29] rendered the molecular docking simulation in detail, treating the drug as a ligand and the protein as a macromolecule. For docking analysis, Autodock-Vina [30] was employed.

## 2.2 Molecular dynamics simulations and MM-GBSA calculations

To verify the binding stability and pose orientation of each candidate hit in the target protein's active site, a molecular dynamics (MD) simulation was run. Each hit candidate's docked pose served as input data for the NAMD v2.14 software [31] with the CHARMM36m force field [32]. A periodic box of TIP3P water molecules with a 10.0 spacing along each dimension encircled the complexes. The system's charge neutrality was preserved by the addition of 0.15 M sodium chloride (NaCl). Constant volume and normal temperature (NVT) (20,000 runs) were used to minimize and equilibrate the complexes for 40 ps (picoseconds), and NPT (constant normal pressure and normal temperature) 100 ns was used for the simulations. The temperature was set to 310 K and the pressure was set to 1 atm. Root-mean-square fluctuations (RMSF), radius of gyration (RoG), solvent-accessible surface area (SASA), and root-mean-square deviation (RMSD) were used to analyze the complexes' thermodynamic stability. Each simulation was

run for approximately 1000 frames. For initial setup and result analysis, we use the CHARMM GUI website and the Visual Molecular Dynamics (VMD) program [33], respectively. The MolAICal software's Molecular Mechanics/General Boltzmann Surface Area (MM/GBSA) method was used to calculate the binding free energy [34].

## 3 Results and discussion

We have obtained fully optimized structures of methimazole (MMI), propylthiouracil (PTU), and 4-methyl-3-[2-(4-nitrophenyl)-1,3-dioxo-2,3-dihydro-1*H*-isoindole-5-amido] benzoic acid (COD30) RB3LYP- Method using the 6-311G (d,p) basis set. The geometric parameters of the optimized methimazole and propylthiouracil (reference/standard) compounds such as the bond lengths and bond angles are presented in Table S1 and COD30 in Table S2. Figure 1 displays the COD30 optimized structure along with standards.

### 3.1 Frontier molecular orbital (FMOs)

With quantum chemical methods, the electrochemical behavior and molecular structures of compounds can be learned. To learn more about the electronic and optical properties of the compounds, the FMOs were analyzed. The energies of the lowest unoccupied molecular orbital (LUMO), in contrast to the energies of the highest occupied molecular orbital (HOMO), can function as an electron acceptor and

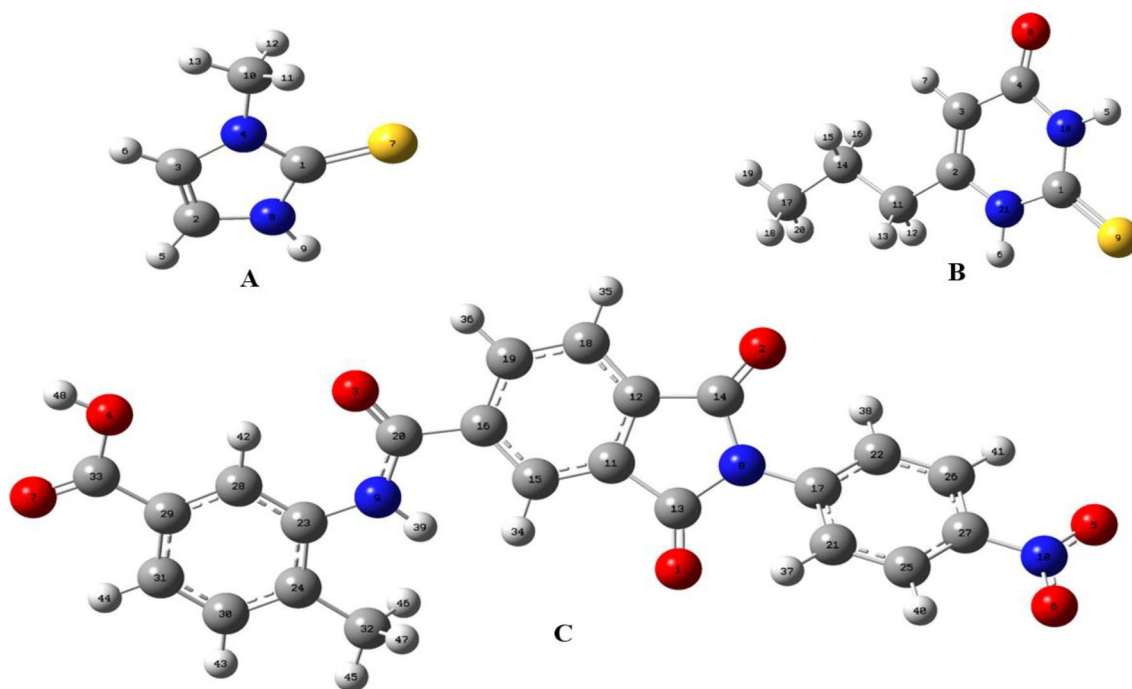


Fig. 1 Optimized structures of A MMI, B PTU, and C COD30 at B3LYP/6-311G (d,p) level

donor, respectively. A key factor in identifying the electrical transport properties of a molecule is the measurement of the energy difference between the lowest unoccupied molecular orbital (LUMO) and the highest occupied molecular orbital (HOMO). This energy gap has a substantial impact on the molecule's chemical and spectroscopic characteristics and is a key indicator of electron conductivity [35]. The HOMO orbitals for compound COD30 were found to have an energy of  $-6.76965$  eV. These energies were contrasted with the corresponding HOMO values for standard methimazole and propylthiouracil, which were  $-5.308$  eV and  $-6.384$  eV, respectively. Compound COD30 had a LUMO energy of  $-3.25278$ . Methimazole and propylthiouracil had LUMO energies of  $+0.130$  and  $-1.567$  eV, respectively. The LUMO–HOMO energy gap ( $\Delta E_{gap}$ ) is a crucial factor in figuring out the characteristics of molecular electric transport and shows how likely a compound is to interact with other molecules. A compound with a small energy gap is more polarizable and typically has a high chemical reactivity and low kinetic stability. COD30, methimazole, and propylthiouracil had values of 3.517, 5.438, and 4.817 eV, respectively. These values indicate the assignable reactivity indices of COD30 with standard methimazole and propylthiouracil. The involvement of each component in HOMO and LUMO is shown in Fig. 2.

When compared to the HOMO diagram, the LUMO diagram of COD30 demonstrated that the electrons were only localized at the isoindoline group regions. The HOMO diagram also demonstrated that the electrons were localized in the upper portion of the formamido and methyl benzoic acid rings. Methimazole and propylthiouracil's LUMO and

HOMO measurements demonstrated that the electrons were localized on the methanethiol ( $-CS$ ) components.

Whether chemical reactions take place within the molecule or involve intermolecular interactions, the degree of electron delocalization between the HOMO and LUMO orbitals is a critical element that dictates their ease and stereo-selectivity. Additionally, a smaller energy difference between the HOMO and LUMO orbitals suggests the possibility of studying intramolecular charge transfer and verifying the molecule's bioactivity [36]. Small energy gaps indicate unstable systems, whereas big gaps indicate stable systems. Molecules with short HOMO–LUMO gaps are more polarizable and reactive, and thus often have lower stability and increased chemical reactivity. Therefore, according to the frontier molecular orbitals (FMO) analysis, COD30 has chemical activity that is noticeably higher than that of common medications [37].

### 3.2 Density of state and partial density of state

A Density of States (DOS) analysis was carried out in conjunction with frontier molecular orbitals utilizing the B3LYP/6-311G (d, p) approach to investigate the electronic characteristics of distinct molecules and give additional analysis for FMOs. With this strategy, we want to clarify and validate the precise traits that FMOs have suggested. The projected/partial density of states (PDOS) and density of states (DOS) spectra computed with GaussSum 3.0 [38] are shown in Fig. 3. The number of states within a specific energy range in a system can be determined with the help of DOS analysis, which also offers insightful information

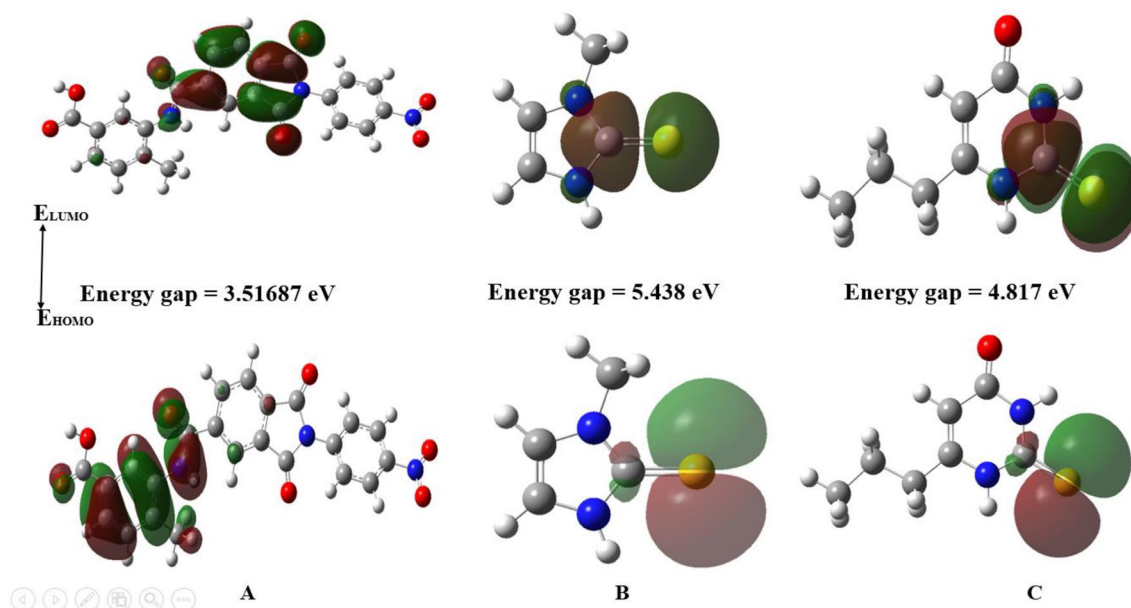


**Fig. 2** Frontier molecular orbitals of **A** COD30, **B** MMI, and **C** PTU and their LUMO-HOMO energy gap (eV)

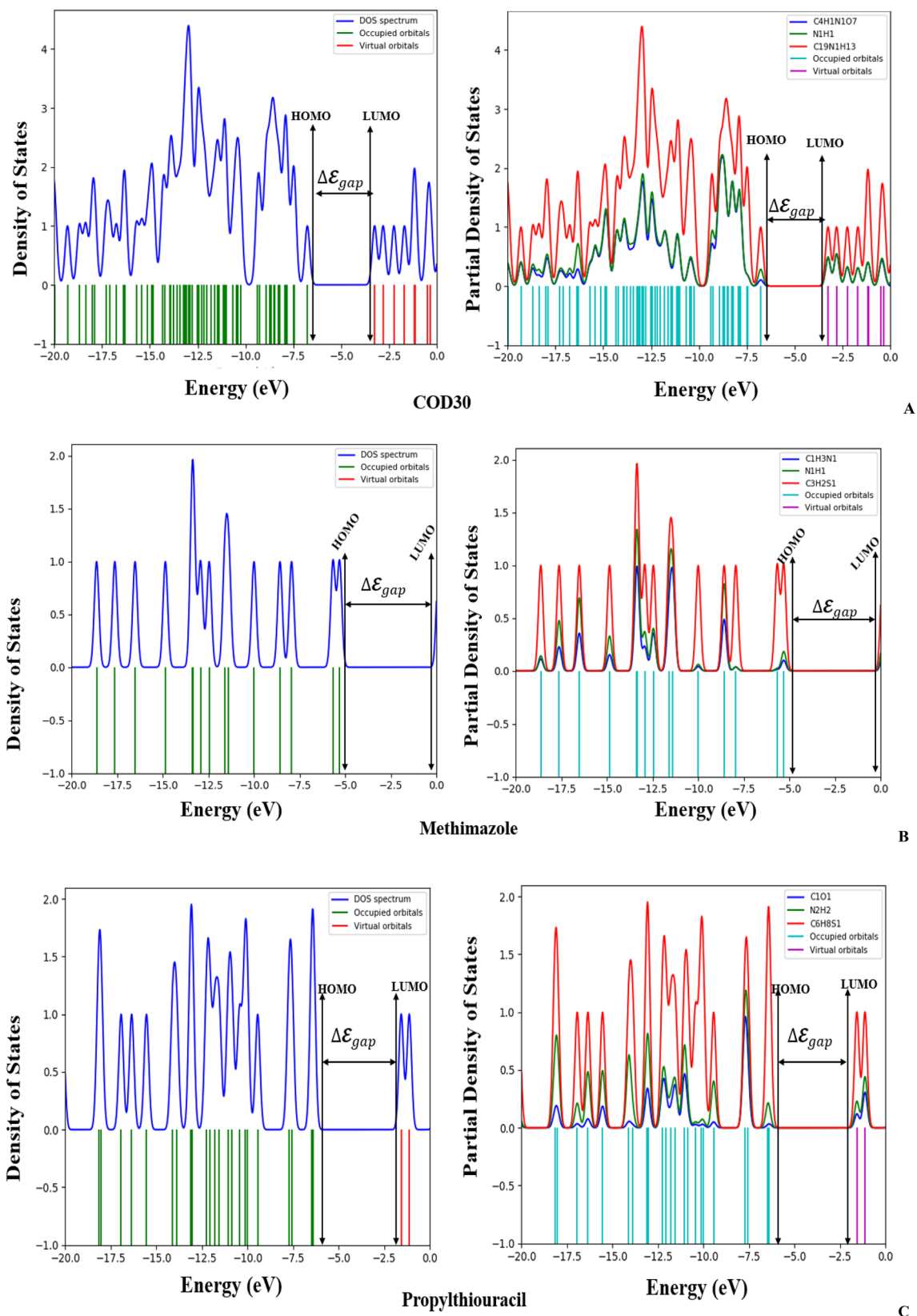


Fig. 3 DOS and PDOS plot and HOMO-LUMO energy gap of the selected compounds



on fragment interactions and the role of molecular orbitals (MO) energy levels in the complex [23]. The proportionate contribution of a particular atom or orbital to the total DOS is represented by PDOS, in contrast [39]. To explore electron and molecule structures during wavefunction analysis, both DOS and PDOS spectra provide visual representations of the interacting components [40]. The GaussSum v3.0 program is a flexible tool that makes it easier to visually explore electron and molecule structures for wavefunction analysis, making the compounds under research easier to examine for DOS and PDOS [23].

The occupied and unoccupied molecular orbitals near the HOMO and LUMO molecular orbitals are the only ones included in the density of state depicted in Fig. 3. The orbital HOMO is represented by the color green, and the orbital LUMO by the colour red. A bonding interaction supported the PDOS's positive value, whereas an anti-bonding interaction contends that negative values and non-binding interactions imply values very near zero. In the boundary zone, neighboring orbitals' quasi-degenerate energy levels could develop. The HOMO orbital is constrained on the rings of formamido and methyl benzoic acid. The confinement of the LUMO orbital on the indoline ring. It's interesting to note that the molecules' wide energy gaps reveal a variety of hydrophilic interactions that may help molecules connect to receptors more easily. This implies that these hydrophilic interactions have a significant impact on the affinity of these medicines for binding to receptors. The HOMO of a certain medication and the LUMO with the surrounding residues may share orbital interactions during the binding process [41]. In addition, it shows us that the molecules have high excitation energies and good stability [42, 43]. It should be noted that reducing the energy gap also boosts chemical reactivity. The molecular orbitals contributing to the fragment orbitals are mostly described by the PDOS. The plots of PDOS, on the other hand, show how each molecular fragment contributed to the orbitals that formed the final molecule. The PDOS graphs show that the HOMO region has the strongest orbital interaction. The three chemicals under study can be grouped according to their ability to donate electrons as follows: Fig. 3A–C. For the investigated substances, the DOS analysis and FMO results agree quite well.

### 3.3 Mulliken atomic charges and Fukui functions

The estimation of partial atomic charges of molecules can be achieved through the utilization of Mulliken charge analysis. Furthermore, the determination of atomic Mulliken charges can identify the adsorption sites of drug molecules. Tables S3 and S4 outline the Mulliken atomic charges of reference compounds such as methimazole, propylthiouracil, and COD30, respectively. Upon analysis of the outcomes, it was evident that the atoms of sulfur, oxygen, and nitrogen

exhibited a predominantly negative charge attributable to molecular relaxation. Meanwhile, the hydrogen atoms displayed positive charges. To specify, the 1O–7O, 8N, 9N, and 32C atoms of COD30 were recognized to possess substantial negative charges that potentially function as active adsorption sites. In general, acceptor molecules can share electrons with heteroatoms (N and O). Moreover, the 13C, 14C, 20C, and 33C atoms in COD30 have the highest positive charges. The Fukui function is one of the most prevalent and basic measures of reactivity. The Fukui function modifies the density function ( $\rho$ ) of a molecule by altering the number of electrons  $N$  within it while maintaining a fixed external potential. Following is a definition of Fukui's function:

$$F(r) = \left( \frac{\partial \rho(r)}{\partial N} \right) r \quad (1)$$

In this equation,  $r$  is the nucleuse's external potential,  $N$  is its electron density, and  $\partial \rho$  is its number of electrons. Fukui functions serve as reactivity descriptors that can be used to locate the most reactive sites in a molecule. Fukui functions determine the tendency of the electronic density to deform at a specific location when electrons are accepted or donated [44]. Condensed or atomic Fukui functions can also be defined for the  $j$ th atomic position as follows:

$$f_j^- = q_j(N) - q_j(N-1) \quad (2)$$

$$f_j^+ = q_j(N+1) - q_j(N) \quad (3)$$

$$f_j^o = \frac{1}{2} [q_j(N+1) - q_j(N-1)] \quad (4)$$

In these equations,  $q_j$  stands for the atomic charge at the  $j$ th atomic site of the neutral ( $N$ ), anionic ( $N+1$ ), or cationic ( $N-1$ ) chemical species, as determined by Mulliken population analysis, electrostatically derived charge, etc. The calculated reactivity order for the electrophilic case was zero (Tables S3 and S4). However, for the nucleophilic attack,  $12C > 2O > 11C > 14C > 16C$  is observed (Table S4).

### 3.4 Global descriptors

By comprehending the connection between a compound's chemical reactivity and its inhibitory effectiveness, comparative studies often employ global chemical descriptors to identify the most reactive sites to determine a compound's inhibitory effectiveness [45]. In addition the fact that  $\mathcal{E}_{HOMO}$ , the outer orbital holding electrons serve as an electron donor, and the ionization potential ( $I$ ) is directly related to the energy of the HOMO.  $\mathcal{E}_{LUMO}$  does, however, possess an electron-accepting capacity, and its electron affinity ( $A$ ) is proportional to its LUMO energy. To calculate global

reactivity descriptors like chemical potential ( $\mu$ ), electronegativity ( $\chi$ ), hardness ( $\eta$ ), softness ( $S$ ), and electrophilic index ( $\omega$ ), HOMO–LUMO energies are used [46]. The following equations are used to calculate quantum chemical descriptors:

$$\text{Ionization potential (I)} = -E_{\text{HOMO}} \quad (5)$$

$$\text{Electron Affinity (A)} = -E_{\text{LUMO}} \quad (6)$$

$$\text{Chemical potential } (\mu) = -(I + A)/2 \quad (7)$$

$$\text{Electronegativity } (\chi) = -(I + A)/2 \quad (8)$$

$$\text{Hardness } (\eta) = -(I + A)/2 \quad (9)$$

$$\text{Softness } (S) = 1/\eta \quad (10)$$

$$\text{Electrophilicity index } (\omega) = \mu^2/2\eta \quad (11)$$

High and low chemical reactivity are correlated with small and large HOMO–LUMO energy gaps ( $\Delta E_{\text{gap}}$ ), an indicator of chemical stability and reactivity. COD30 has the highest reactivity and inhibition efficiency due to its low HOMO–LUMO gap value, while methimazole, has the lowest reactivity because of its high energy gap ( $\Delta E_{\text{gap}}$ ). As a result of the  $-C7H3OOH$  and  $-CONH$  groups, COD30 is more chemically reactive. The two reference drugs methimazole and propylthiouracil showed the highest softness and hardness values respectively. The highest chemical hardness and lowest chemical softness values are consistently associated with COD30, which had the highest reactivity. According to the literature [47], the highest electronegativity is related to high chemical reactivity (or lowest  $\Delta E_{\text{gap}}$ ). Based on our findings (Table 1), COD30 has the lowest  $\Delta E_{\text{gap}}$ , the highest electronegativity, and the highest global electrophilicity, showing a high ability to accept electrons.

## 4 NB: energy value (eV)

### 4.1 Molecular electrostatic potential (MEP)

MEP displays a molecule's electron density, and it can be used to locate electrophilic and nucleophilic attack sites [48] and hydrogen bonding sites [49]. In the ESP bar, various colors represent different electrostatic potential values, which are frequently used to determine the distribution of electronic charges. Electrophilic reactivity is represented by red, followed by yellow and orange, while nucleophilic reactivity is represented by blue, followed by green [50]. The highest electron density is found in the  $-CO-$  groups,

**Table 1** HOMO and LUMO energies (eV), energy gap, and global descriptors of the selected ligands

Molecular descriptors	Methimazole	Propylthiouracil	COD30
HOMO energy	− 5.3080	− 6.384	− 6.7697
LUMO energy	0.1300	− 1.567	− 3.2528
Energy gap	5.438	4.817	3.5169
Ionization potential (I)	5.3080	6.384	6.7697
Electron affinity(A)	− 0.1300	1.5670	3.3528
Electronegativity ( $\chi$ )	3.3936	4.0436	5.0123
Chemical potential ( $\mu$ )	− 3.3936	− 4.0436	− 5.0123
Chemical Hardness ( $\eta$ )	3.2629	3.4776	3.5184
Chemical softness (S)	226.9318	212.9049	210.5318
Electrophilicity index ( $\omega$ )	1.7665	2.3518	3.5699

while the phenyl and bicyclic groups have a nucleophilic attacked region, as shown in Fig. 4. These results are crucial for understanding how a compound's electrophilic and nucleophilic reactivity relate to one another. Reactive electrophilic and nucleophilic sites are located in a manner that is consistent with FUKUI functional analysis.

### 4.2 Thermochemistry properties

The thermochemical properties and contribution of thermochemical quantities for each frequency mode of methimazole, propylthiouracil, and COD30. These values were calculated using Shermo software v2.2 [51] using normal conditions of temperature (298.15 Kelvin) and pressure (1 atm). The values such as zero-point energy (ZPVE), internal energy (U), entropy (S), enthalpy (H), Gibbs free energy (G), molar heat capacity at constant volume ( $C_v$ ), and heat capacity at constant pressure ( $C_p$ ) of the compounds are listed in Tables S5–S10. The partition function ( $q$ ), which plays a key role in statistical thermodynamics, is also studied. We observe a very high variation in the sum of the translational, rotational, vibrational, and electronic energies for each of these three compounds, as presented in the supplemental material. The COD30 is energetically stable when presenting negative electronic energy, since the more negative values, the more stable and favorable the formation of the compound. Therefore, the most stable complex is the COD30, while the least stable is the MMI. The positive enthalpy values describe the non-covalent interactions generated. On the other hand, the positive entropy values describe the limitation of rotational and translational motion of the ligand.

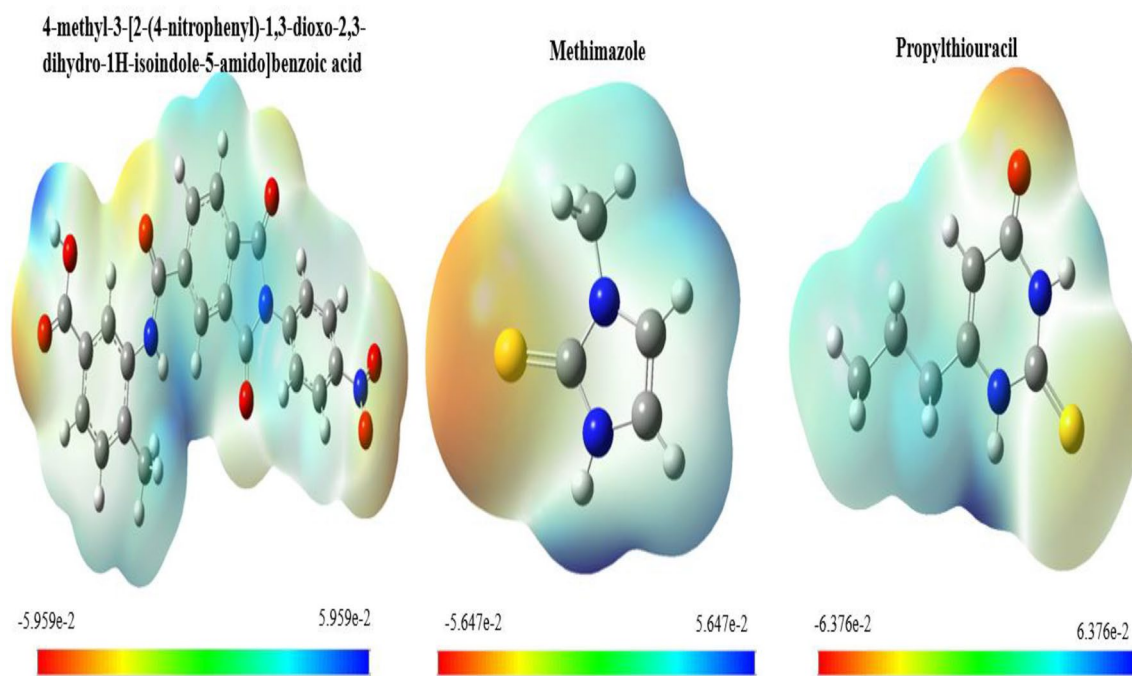


Fig. 4 Molecular electrostatic potential [MEP (eV)] of COD30, MMI, and PTU.

### 4.3 Vibrational analysis

The vibrational frequencies, the vibrational mode assignments, and the potential energy distributions (PED) of COD30, methimazole, and propylthiouracil compounds at B3LYP level with 6-311G(d,p) basis set were calculated and IR spectra are shown in Fig. 5 and Tables 2, S11, S12, respectively. These results were selected from the calculated infrared spectra obtained. There are 138 vibrational modes in the range of  $9.73\text{--}3773.07\text{ cm}^{-1}$  donated by B3LYP/6311G (d, p), which donates COD30 with 48 atoms (3N-6). Methimazole with 13 atoms thus donates (3N-6) 33 vibrational modes in the range  $75.19\text{--}3670.52\text{ cm}^{-1}$  (Table S11). Propylthiouracil with 21 atoms thus donates (3N-6) 57 vibrational modes in the range  $52.46\text{--}3612.89\text{ cm}^{-1}$  (Table S12). To establish a correlation between structure and spectrum, their vibrational modes were assigned. 47 stretching modes, 46 bending modes, and 45 torsional modes are distinguished by the vibrational modes of COD30. There are 39 different CH modes. The vibrational modes of methimazole are 12 stretch modes, 11 bending modes, and 10 torsion modes, the number of CH modes is 15. The propylthiouracil vibrational modes are 20 stretches, 19 blending/flexure, and 18 torsion modes. The total number of CH modes is 24. The high-frequency region of the IR spectrum is therefore largely dominated by the broad OH and NH stretching vibration, with weaker bands originating from the CNCC torsional modes. This conclusion is supported by an analysis of the

IR spectra shown in Fig. 5 and Table 2 of COD30. The frequency at which the CH stretches were seen ranged from  $3007\text{ to }3186\text{ cm}^{-1}$ . Alkanes and aromatic structures' CH stretching vibrations are known to be localized in the regions of  $2850\text{--}3000\text{ cm}^{-1}$  and  $3000\text{--}3100\text{ cm}^{-1}$ , respectively, according to the literature [52–60]. The experimental data in the literature and this value are in agreement. Secondary amides' free NH stretches are typically found in the range of  $3300\text{--}3460\text{ cm}^{-1}$  [54–60]. The NH stretching vibration is represented by the strong broadband at  $3326\text{ cm}^{-1}$  in the IR spectrum. The wave number for this band, according to DFT calculations, is  $3645\text{ cm}^{-1}$ . In the IR spectrum, the C=O bond results in distinctive bands that span the wavelength range of  $1730\text{--}1750\text{ cm}^{-1}$  [53–60]. In good agreement with the experimental data, we observe a C=O stretching vibration in COD30 in the frequency range  $1752\text{--}1794\text{ cm}^{-1}$ . Infrared spectra with frequency ranges between  $326\text{ and }528\text{ cm}^{-1}$  show the symmetry bending modes for OOC. A frequency of  $528\text{ cm}^{-1}$  was used to observe the asymmetric bending modes for OCO.

### 4.4 Docking simulations results

Structure-based drug design uses molecular docking to examine how a small molecule interacts with a protein at the atomic level. For each target, Table 3 shows the results of the docking simulation for compound COD30 and the reference drugs. The findings demonstrated that COD30, the subject



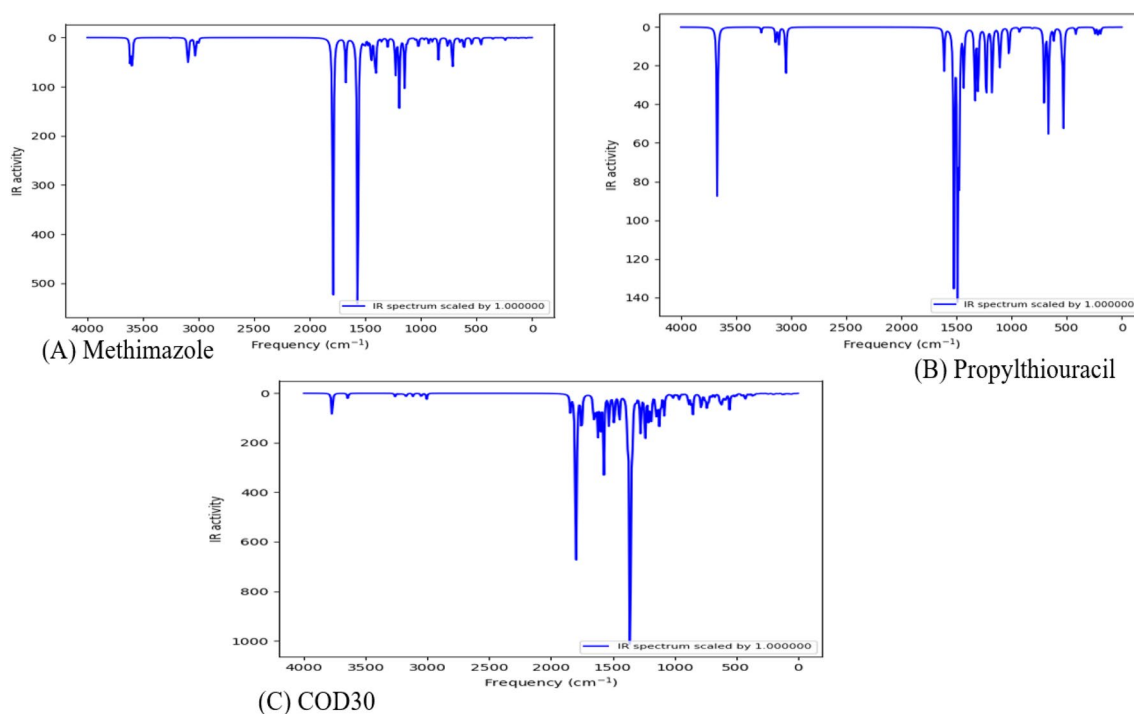


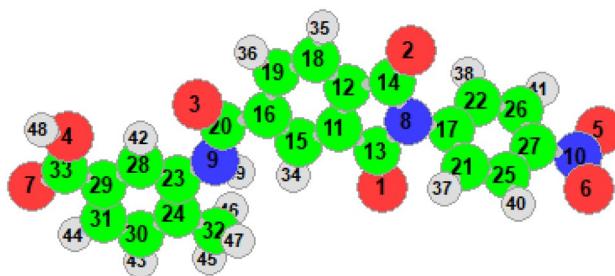
**Fig. 5** The IR spectrum of **A** methimazole, **B** propylthiouracil, and **C** COD30 obtained using B3LYP by employing the 6-311G (d,p) basis set

of the investigation, had the highest docking scores when compared to the reference drugs. In studies, amino acid residues at protein active sites and bound compounds have been examined using protein–ligand interaction plots [61–63]. As a result of this study, Fig. 6 illustrates the interactions that were found between the compounds and amino acid residues in the active sites of each target protein. To examine ligand-receptor interactions and ligand stability, 10 ns MD simulations were conducted against PTPN22 (4j51.pdb). Additionally, calculations using the MM-GBSA method were done in this section to precisely calculate the binding free energies. Figures 7 and 8 display the MD simulation trajectory and the 2D ligand-receptor interactions for each ligand after the 100 ns MD simulation, respectively.

#### 4.5 MM/GBSA results

The COD30 and MMI complexes had the lowest calculated binding free energies (Table 4), resulting in the strongest binding affinities. These values were  $-177.3849$  and  $-236.9114$  kcal/mol. According to the findings, the MMI complex system's primary force was the van der Waals force. Also, the van der Waals force was crucial in bringing COD30 and PTPN22 receptors together. PTU and the macromolecule PTPN22 had a calculated binding free energy of 18.8833 kcal/mol. The van der Waals force was significantly less powerful than the electrostatic interaction. Figure 7A displays the RMSD for the three complexes. RMSD

fluctuates of the three complexes were all in a very small range which indicated that the systems had reached a state of stability. It was discovered that the average RMSD of COD30, MMI, and PTU with 4j51.pdb protein was 0.995, 1.052, and 1.1, respectively. The average RMSD of the COD30 complex was slightly lower than that of the MMI and PTU complexes, meanwhile, all the complexes are in the acceptable range. Additionally, the visual analysis of the trajectories demonstrated that the systems had reached equilibrium, providing initial proof that systems are stable under physiological conditions. The radius of gyration (RoG) plot was measured (Fig. 7B). The RoG imparts the compactness of a structure throughout the simulation. The RoG-time fluctuations were observed almost constants within the acceptable range, mostly maintained between 20 and 20.2 Å, indicating steady conformation changes in the protein. Table 4 shows that MMI-4j51.pdb has marginally lower RoG values, however, the difference cannot be considered significant. The obtained results revealed that the complexes could keep stable throughout the simulation and interact well with the PTPN22 protein. With an average RMSF of 0.6, the protein's fluctuation profile (Fig. 7C) reveals that there is not much movement, demonstrating the stability of the interactions between the drugs (COD30 and MMI) and the PTPN22 protein (4J51.pdb). The SASA analysis was explored to determine the solvent accessibility of the complex (Fig. 7D). The SASA of the COD30 complex fluctuated at about 5–7.5 ns during the MD simulations and the average value of SASA

**Table 2** Vibrational frequencies in  $\text{cm}^{-1}$  of COD30

IR	Raman	$\text{cm}^{-1}$	Modes/potential energy distribution (PED%)
103.43	202.77	3773.07	$\nu$ OH (100)
22.52	172.12	3645.44	$\nu$ NH (100)
13.80	28.83	3263.70	$\nu$ CH (99)
1.54	140.21	3238.15	$\nu$ CH (74) + $\nu$ CH (20)
1.32	7.63	3237.49	$\gamma$ CH (77) + $\gamma$ CH (17)
1.26	71.80	3224.28	$\nu$ CH (18) + $\gamma$ CH (82)
1.27	33.06	3223.01	$\gamma$ CH (22) + $\nu$ CH (78)
0.84	147.53	3210.08	$\nu$ CH (94)
1.39	150.09	3208.77	$\nu$ CH (96)
1.48	71.21	3197.22	$\nu$ CH (94)
5.48	53.00	3185.64	$\nu$ CH (99)
13.81	112.04	3171.70	$\nu$ CH (96)
13.39	79.57	3116.86	$\nu$ CH (92)
16.87	70.18	3050.39	$\nu$ CH (100)
23.92	179.25	3006.69	$\nu$ CH (92)
71.42	480.32	1842.58	$\nu$ OC (83)
387.65	76.52	1801.22	$\nu$ OC (83)
527.95	8.88	1794.3	$\nu$ OC (85)
189.24	273.43	1751.56	$\nu$ OC (80)
16.42	244.17	1655.52	$\gamma$ CC (47)
84.82	14.12	1654.29	$\gamma$ CC (52)
14.48	820.10	1652.85	$\gamma$ CC (50)
46.05	580.95	1640.46	$\nu$ CC (43) + $\beta$ HCC (15)
44.53	115.57	1635.16	$\nu$ CC (40) + $\nu$ CC (13)
156.80	475.11	1619.22	$\nu$ CC (46)
148.45	8.65	1597.21	$\nu$ ON (78) + $\gamma$ CC (10)
350.26	392.51	1572.75	$\nu$ NC (11) + $\beta$ HNC (39)
133.19	56.30	1529.50	$\nu$ CC (10) + $\beta$ HCC (56) + $\beta$ CCC (14)
0.81	0.74	1519.22	$\beta$ HCC (20) + $\delta$ HCH (27)
2.66	21.13	1509.78	$\beta$ HCC (45)
10.39	11.46	1495.56	$\delta$ HCH (76) + $\tau$ HCCC (17)
146.23	92.34	1487.75	$\delta$ HNC (13) + $\beta$ HCH (34)
4.74	139.22	1455.08	$\gamma$ CC (51) + $\delta$ HCC (15)
1.79	8.88	1451.07	$\gamma$ CC (36) + $\beta$ HCC (31)
130.02	273.73	1445.91	$\nu$ CC (56)
0.61	10.02	1415.02	$\beta$ HCH (91)
0.67	15.93	1386.64	$\gamma$ NC (53)
139.53	36.60	1380.85	$\nu$ CC (13) + $\beta$ HOC (32)
12.95	165.08	1376.77	$\nu$ CC (34)

Table 2 (continued)

IR	Raman	cm <sup>-1</sup>	Modes/potential energy distribution (PED%)
1409.34	2391.15	1359.44	ν NC (59) + δ CNC (10)
17.88	1.26	1354.25	ν CC (65) + β HCC (14)
198.32	102.88	1341.92	γ CC (62)
2.16	0.91	1329.09	δ HCC (76)
21.53	112.67	1309.73	β HCC (67)
1.36	1.31	1295.94	δ HCC (63)
151.83	1088.85	1275.47	γ NC (47) + β HNC (13)
12.80	77.49	1265.38	γ CC (43)
222.99	13.69	1237.29	γ NC (32) + δ HCC (11)
97.90	5.42	1209.50	γ CC (10) + β HCC (17) + δ CCN (14)
2.14	8.54	1207.20	ν CC (22) + δ HCC (65)
71.08	27.95	1194.90	γ CC (12) + β HOC (11) + β HCC (13)
84.12	24.36	1186.04	γ CC (17) + β HCC (12) + β HCC (17) + β HCC (11)
87.97	14.93	1149.27	γ CC (20) + β HCC (18)
38.05	1.28	1140.83	ν CC (13) + β HCC (59)
19.98	19.71	1131.19	ν NC (10)
84.14	269.97	1121.38	ν NC (52)
39.16	62.02	1120.24	β HCC (26)
37.41	35.56	1107.06	γ OC (48) + β HCC (11)
6.83	23.79	1086.39	δ HCC (10) + β CCC (21)
81.23	1081.79	1081.79	γ NC (54)
2.69	0.33	1058.87	δ HCH (21) + ω HCCC (33) + τ HCCC (26)
3.23	21.05	1031.66	δ HCC (18) + β CCC (74)
7.26	1.75	1013.69	ω HCCC (64)
14.30	19.22	1012.35	ω HCCC (50)
0.60	0.11	991.97	τ HCCC (84) + τ CCCC (13)
0.35	0.41	986.24	τ HCCC (75)
4.96	2.03	985.77	τ HCCC (87)
9.83	1.04	964.22	τ HCCC (74)
17.49	10.39	959.74	ν CC (15)
2.36	23.40	955.30	γ NC (10) + β CCC (14)
3.40	1.16	928.54	τ HCCC (69)
7.49	6.76	890.32	τ HCCC (73)
22.20	21.09	884.14	β OCN (18)
19.63	26.98	883.04	ν NC (27) + β ONO (28)
34.94	2.75	866.89	ω HCCC (66)
4.26	0.49	859.06	ω HCCC (71) + σ OCOC (13)
83.43	3.48	850.77	γ CC (12) + γ NC (10) + δ ONO (23)
0.10	6.95	838.04	τ HCCC (97)
2.94	12.85	802.07	π OCNC (58)
3.95	21.28	790.63	γ CC (23) + β CCC (26)
52.82	2.95	783.23	τ HCCC (15) + σ OCNC (14) + σ OCOC (43)
20.21	7.21	779.75	σ OCNC (44) + π OCOC (17)
19.26	4.07	754.79	π OCON (49)
36.22	14.27	740.36	σ OCNC (35)
4.81	17.86	737.47	ν CC (15) + δ CCC (33) + δ ONO (10)
25.19	10.33	734.67	σ OCON (22)
1.62	0.90	730.44	ω CCCC (51)
36.01	2.96	724.37	γ CC (32) + γ CC (13) + β CCC (14)
13.24	0.30	699.32	ω HCCC (15) + τ CCCC (67)

Table 2 (continued)

IR	Raman	cm <sup>-1</sup>	Modes/potential energy distribution (PED%)
2.73	10.21	676.04	$\tau$ CCCC (13)+ $\tau$ CCCC (17)+ $\sigma$ OCNC (10)
11.70	20.09	671.98	$\tau$ CCCC (10)+ $\tau$ CCCC (12)
1.01	7.44	644.06	$\beta$ CCC (61)
22.72	9.44	632.53	$\delta$ OCO (40)
51.74	5.59	620.95	$\tau$ HOCC (80)
18.08	2.88	611.56	$\nu$ NC (10)+ $\beta$ CNC (15)
22.94	21.10	595.87	$\beta$ CCN (42)
23.95	27.74	582.52	$\beta$ CCN (28)+ $\omega$ HNCC (12)
63.66	4.44	553.03	$\omega$ HNCC (69)
3.57	18.41	541.75	$\omega$ HOCC (56)
0.56	2.51	536.43	$\beta$ CNO (69)
5.30	1.38	528.24	$\beta$ CCO (69)
10.37	0.65	513.22	$\tau$ CCCC (77)
8.87	9.32	498.13	$\pi$ CCCC (10)+ $\pi$ CCCC (14)
0.47	0.65	473.72	$\gamma$ NC (10)+ $\beta$ CCC (13)
12.96	1.50	452.92	$\omega$ CCCC (73)
9.82	0.80	430.76	$\omega$ CCCC (14)+ $\pi$ CCCC (12)
16.79	0.83	423.50	$\omega$ CCCC (12)
1.76	9.58	421.11	$\delta$ CCC (38)+ $\omega$ CCCC (28)
1.82	3.31	418.78	$\beta$ CCC (16)+ $\omega$ CCCC (43)
5.70	0.28	393.23	$\beta$ NCC (29)
10.78	5.41	366.79	$\beta$ OCC (12)
6.74	3.85	351.21	$\nu$ CC (36)
0.13	0.57	329.37	$\omega$ CCCC (19)+ $\omega$ CCCC (10)
1.37	1.31	325.60	$\beta$ OCC (14)+ $\sigma$ CCCC (12)
1.42	2.24	315.64	$\sigma$ CCCC (26)
0.84	3.45	282.15	$\delta$ CCC (10)+ $\delta$ CNC (24)
0.09	4.82	260.29	$\beta$ CNC (11)+ $\sigma$ CCCC (16)
2.16	3.27	244.49	$\beta$ CCN (27)
2.03	0.48	236.68	$\delta$ CNC (29)
0.91	2.17	211.72	$\delta$ CCN (11)+ $\pi$ CCCC (11)+ $\tau$ CCCN (31)
3.22	0.75	202.02	$\delta$ CNC (33)
0.53	0.61	196.97	$\tau$ HCCC (47)+ $\tau$ HCCC (25)+ $\sigma$ CCCC (10)
3.25	0.54	189.45	–
1.49	0.98	163.39	$\sigma$ CCCN (32)
0.92	5.10	154.53	$\omega$ CCCC (53)
6.25	0.29	123.48	$\sigma$ CCCN (22)+ $\omega$ CCCC (16)
3.00	1.53	106.36	$\omega$ CCCC (11)
0.08	0.79	102.60	$\sigma$ CCCC (76)
0.47	0.52	90.89	$\beta$ CNC (49)
2.10	2.46	79.16	$\omega$ CNCC (60)
1.27	4.86	65.34	$\tau$ CNCC (88)
1.23	1.77	57.10	$\omega$ CCCC (19)+ $\tau$ CCCC (15)
3.11	1.76	50.77	$\tau$ CCCC (59)
0.28	1.16	38.78	$\tau$ CCNO (49)
0.67	2.73	36.29	$\tau$ CCNO (27)+ $\tau$ CCNC (26)
0.57	3.58	23.89	$\tau$ CCNC (34)
0.19	6.16	17.97	$\tau$ CCCC (12)+ $\tau$ CNCC (12)+ $\omega$ CCNC (16)+ $\sigma$ CCCC (10)+ $\pi$ CCCC (11)
0.53	2.43	9.73*	$\omega$ CNCC (62)

$\nu$  symmetry stretching,  $\gamma$  asymmetry stretching,  $\beta$  symmetry bending,  $\delta$  asymmetry bending,  $\tau$  symmetry torsion,  $\omega$  asymmetry torsion,  $\sigma$  symmetry out of plane,  $\pi$  asymmetry out of plane



**Table 3** The binding affinity, estimated inhibition constant, and ligand efficiency of the investigated compounds

Receptors	<sup>A</sup> 4j51.pdb			<sup>B</sup> 1nav.pdb			<sup>C</sup> 1nax.pdb		
	$\Delta G$	Est. Ki	LE	$\Delta G$	Est. Ki	LE	$\Delta G$	Est. Ki	LE
COD30	- 10.2	33.37 nM	0.31	- 8.9	299.41 nM	0.27	- 7.9	1.62 uM	0.24
Meth	- 4.0	1.17 mM	0.57	- 4.2	0.83 mM	0.60	- 3.9	1.38 mM	0.56
Propyl	- 5.6	78.56 uM	0.51	- 6.2	28.53 uM	0.56	- 6.2	28.53 uM	0.56

was found to be 16,689.45 Å<sup>2</sup> (Table 4). Furthermore, the SASA plot revealed that the structure of the PTU complex was relatively unstable during the simulation time.

We docked three anti-graves' disease, COD30, MMI, and PTU, into the selected crystal protein structures, as shown in Fig. 6. Comparing Fig. 6A's, the highest docked protein, we found some similarities of the binding between these three ligands. The amino acid residues LYS39, TYR66, and SER35, formed hydrogen bonds, hydrophobic, and van der Waals interactions with these three ligands. We compared the changes in binding modes and interactions of the selected ligands after MD simulations. Figure 8 shows the detailed interactions between the PTPN22 protein (4J51.pdb) and these ligands. Some of the key interactions observed in the complexes from the docking analysis were preserved in the molecular dynamics simulation complexes as shown in the analysis of the representative structures. The TYR44 conventional hydrogen bond interaction with COD30. The TYR66 conventional hydrogen bond interaction with COD30 and PTU, ASP195, and ASP62 hydrogen bond interaction with MMI and PTU was observed in the representative structures. Other interactions stabilizing the complexes are hydrophobic such as the LYS39, LEU281, LYS42, and TYR66.

#### 4.6 Bioactivity of the COD30 compound and the standards

To evaluate the quality of the molecules, several parameters were calculated, including Ligand Efficiency (LE), Ligand Efficiency Scale (LE<sub>scale</sub>), Quality of Fit (FQ), and Ligand Efficiency-dependent Lipophilicity (LELP). According to research, the similarity parameter LE can be calculated using equation [64–66]. It is a ratio of the number of heavy atoms in a hit to the negative binding energy. To describe a hit's lead-like characteristics, LE values of 0.3 should be used. In this instance, all of the compounds had LE values of 0.31, 0.57, and 0.51, which indicated that all were lead-like molecules (Table 3).

$$LE = \frac{-\Delta G}{HA} \quad (12)$$

Ligand lipophilic efficiency (LLE) is a measure of how effectively a substance binds to a target protein or produces its potency (Eq. 13). In other words, it assesses how

effectively compounds maintain low lipophilicity while enhancing potency [64].

$$LLE = pKi - \log D \quad (13)$$

According to a report, a promising drug candidate should have a lipophilic efficiency greater than 5 and Log P values between 2 and 3. None of the standard treatments for Graves' disease satisfies these criteria, except COD30 displays values over 5. The reference medicines display values that are just above 3. Following Lipinski's rule of five, we also noted that the Log P values of all the compounds under study were all found to be lower than 5. The compound methimazole has the lowest Log P (- 0.095), indicating that it has a hydrophilic nature and poor cell membrane permeability. The second parameter is known as LE<sub>Scale</sub> and can be evaluated using Eq. 14, according to Reynolds et al. [65]. The comparison of the small molecule according to size is shown by the LE<sub>Scale</sub>. The potentiality of the molecule is indicated by the LE<sub>Scale</sub> values of COD30, MMI, and PTU, which were found to be 0.3062, 0.6637, and 0.5919, respectively, as shown in Table 5.

$$LE_{scale} = 0.873 \times e^{-0.026 \times HA} - 0.064 \quad (14)$$

Equation 15 can be used to calculate the Fit Quality Score for a well-binding molecule in the receptor. The suggested value for a hit is less than 0.8. Low fit quality scores are a sign of suboptimal binding, while scores close to 1.0 or above are indicative of near-optimal ligand binding, according to Reynolds et al. [65]. In Table 5, the FQ values for COD30, MMI, and PTU are 1.012, 0.859, and 0.862, respectively. In comparison to the standards, CID30 has a strong ability to bind to the graves' disease.

$$FQ = \frac{LE}{LE_{scale}} \quad (15)$$

Equation 16 can be used to calculate the ligand efficiency-dependent lipophilicity index's (LELP) value. LELP, which was proposed by Keseru and Makara [66], is the ratio between logP and LE. Ideal LELP values for derivations were given as ranges between -10 and 10 [67]. It was discovered that COD30, MMI, and PTU had LELP values of 10.6, - 0.167, and 1.833, respectively. As a result, the LELP values in the table above show that all molecules possess drug-like characteristics.

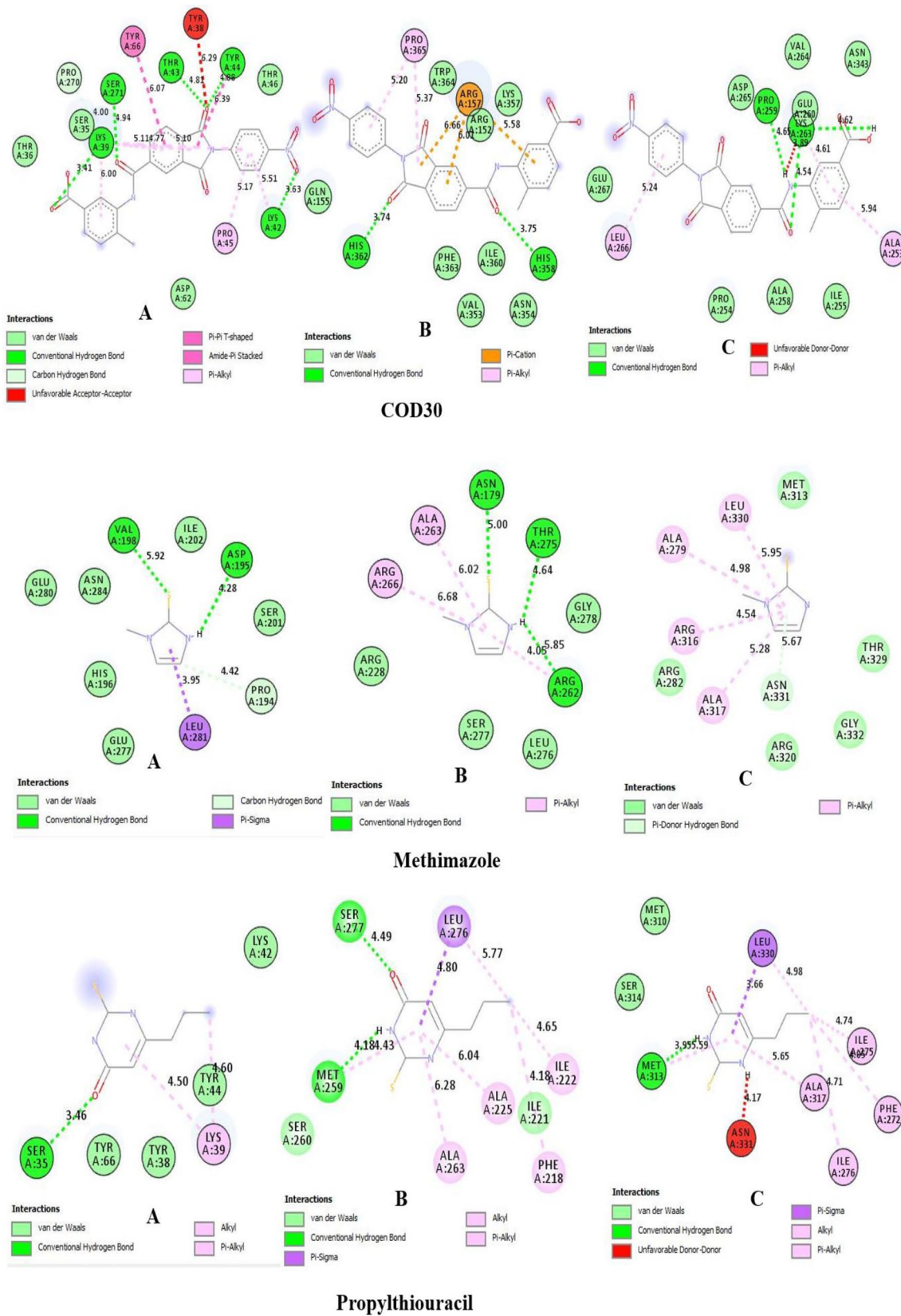


**Fig. 6** The molecular interactions of COD30, MMI, and PTU again **A** PTPN22 (4J51.pdb), **B** THRA1 (1NAV.pdb), and **C** ERBA2 (1NAX.pdb)

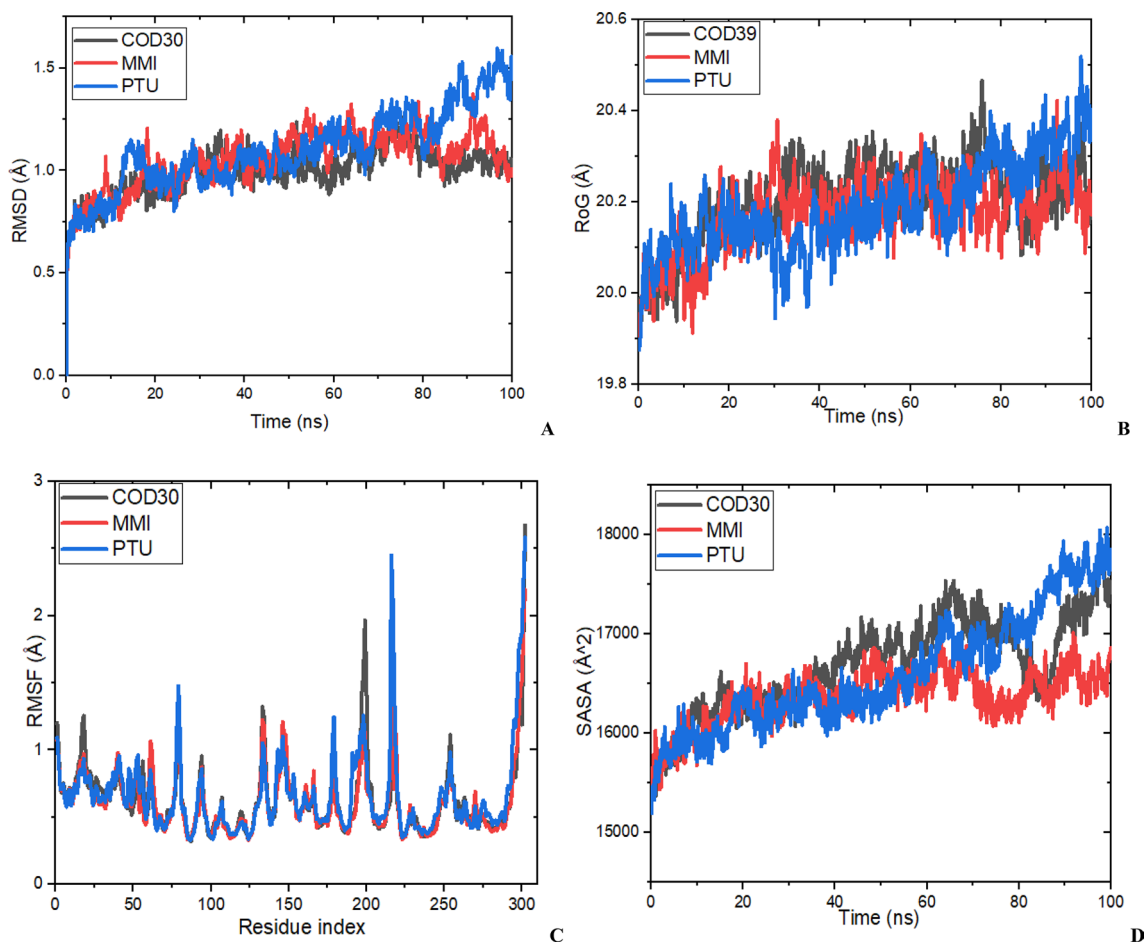


**Fig. 7** **A** Root-mean square deviation (RMSD) of C  $\alpha$  atoms of each complex, **B** radius of gyration (RG) of each complex course of 100 ns of simulation time, **C** root mean square fluctuation (RMSF) of each

complex, and **D** solvent accessible surface area (SASA) of COD30, MMI, and PTU complex as a function of time

$$LELP = \frac{\text{Log}P}{LE} \quad (16)$$

Oral absorption percentage (%ABS) was calculated according to the method of Zhao et al. [68] using the following equation:

$$\%ABS = 109 - (0.345 \times TPSA) \quad (17)$$

where TPSA was the topological polar surface area. We can notice that they all exhibited a great percentage of absorption (%ABS) ranging from 58 to 101%, indicating that these compounds especially COD30 have good cellular plasmatic membrane permeability.

## 5 Conclusion

The geometric parameters, vibrational harmonic frequencies, PED assignments, and molecular orbital energies of COD30 were calculated using DFT (B3LYP) methods with

a 6-311G (d, p) basis set. Our ability to assess how hydrogen bonding affects vibrational frequencies and enhance assignment accuracy was made possible by COD30's hydrogen bonding geometry. Our thorough PED% analysis of the molecule revealed good concordance with the literature. The molecule's HOMO, LUMO, and gap energies are also provided. The most negative and positive surface areas of the compounds under investigation were also revealed by the molecular electrostatic potential study, which allowed researchers to predict the best location for a hydrogen bonding site. According to a molecular docking analysis, COD30's docked poses with the graves' disease receptors displayed a higher binding affinity and significant nonbonding interactions than the reference drugs. The application of anti-grave disease drugs as anticipated inhibitors of PTPN22, THRA1, and ERBA2, which may lessen the thyroid receptor, is suggested by these blind molecular docking studies as a possible strategy. The COD30 and corresponding target receptors could form stable complexes, according to the MD simulation and MM/GBSA calculation. According to the

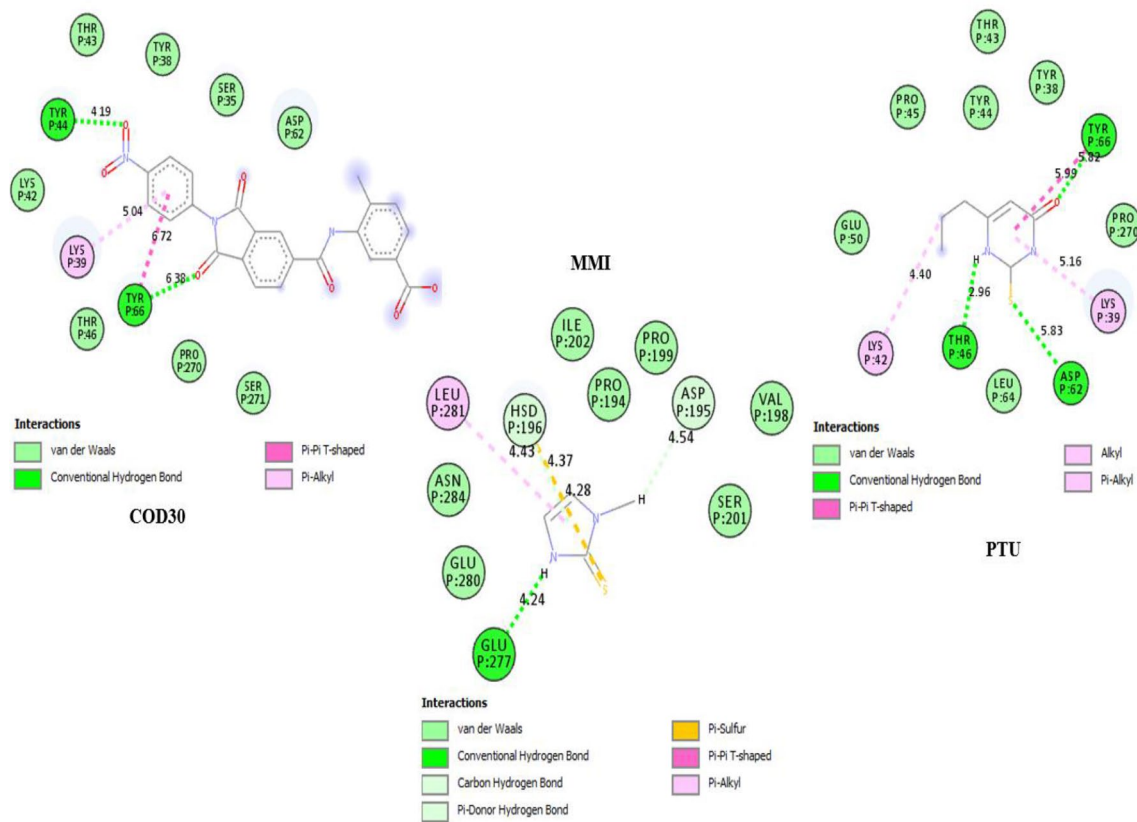


**Fig. 8** Representations of ligand-receptor interactions at the end of 10 ns MD simulations

**Table 4** The MM-GBSA calculations and the average MD simulations parameters

Parameters	COD30	MMI	PTU
Delta E (internal)	- 26.8862	- 96.2912	27.49
Delta E (electrostatic) + Delta G (sol)	- 67.5477	- 43.0867	- 5.6318
Delta E (VDW)	- 82.9509	- 97.5334	- 2.9749
Delta G binding	- 177.3849 ± 5.6171 (kcal/mol)	- 236.9114 ± 5.7034 (kcal/mol)	18.8833 ± 5.9217 (kcal/mol)
Av. RMSD	0.995 Å	1.052 Å	1.100 Å
Av. RoG	20.203 Å	20.172 Å	20.189 Å
Av. RMSF	0.627 Å	0.613 Å	0.654 Å
Av. SASA	16,689.45 Å <sup>2</sup>	16,362.78 Å <sup>2</sup>	16,599.60 Å <sup>2</sup>

**Table 5** Bioactivity analysis of COD30 and the reference drugs

S/n	LogD	LogP	TPSA	pKi	LLE	LE_scale	FQ	LELP	%ABS
COD30	1.879	3.275	146.92	7.4766	5.5976	0.3062	1.0125	10.5645	58.3126
MMI	- 0.162	- 0.095	20.72	2.9318	3.0938	0.6637	0.8588	- 0.1667	101.8516
PTU	1.008	0.935	48.65	4.1048	3.0968	0.5919	0.8617	1.8333	92.21575



bioactivity study, COD30 has superior pharmacokinetic and pharmacodynamic characteristics to those of standard drugs.

**Supplementary Information** The online version contains supplementary material available at <https://doi.org/10.1007/s43994-024-00132-2>.

**Acknowledgements** The authors thank the G.F.S. Harrison Quantum Chemistry Research Group for their valuable support. The authors also express their gratitude to Dr S.N. Adawara.

**Author contributions** EIE and GAS formulated, conceptualized, and designed the research. EIE and MTI did the program using software, organized the data, and analyzed the result. EIE wrote the final drafts of the paper. EIE performed MD simulation. AU, PAM, and GAS reviewed and edited the language of the draft. All authors accepted the final draft and are responsible for the manuscript's content and similarity index.

**Funding** This work receives no financial support from any institution or agency.

**Data availability** None.

## Declarations

**Conflict of interest** The authors declare that they have no known competing financial interests or personal relationships which have or could be perceived to have, influenced the work reported in this article.

**Open Access** This article is licensed under a Creative Commons Attribution 4.0 International License, which permits use, sharing, adaptation, distribution and reproduction in any medium or format, as long as you give appropriate credit to the original author(s) and the source, provide a link to the Creative Commons licence, and indicate if changes were made. The images or other third party material in this article are included in the article's Creative Commons licence, unless indicated otherwise in a credit line to the material. If material is not included in the article's Creative Commons licence and your intended use is not permitted by statutory regulation or exceeds the permitted use, you will need to obtain permission directly from the copyright holder. To view a copy of this licence, visit <http://creativecommons.org/licenses/by/4.0/>.

## References

- Zimmermann MB, Boelaert K (2015) Iodine deficiency and thyroid disorders. *Lancet Diabetes Endocrinol* 3(4):286–295. [https://doi.org/10.1016/S2213-8587\(14\)70225-6](https://doi.org/10.1016/S2213-8587(14)70225-6)
- Davies TF, Andersen S, Latif R, Nagayama Y, Barbesino G, Brito M, Eckstein AK, Stagnaro-Green A, Kahaly GJ (2020) Graves' disease. *Nat Rev Dis Prim* 6(1):52. <https://doi.org/10.1038/s41572-020-0184-y>
- Amin Yavari SA, Castenmiller SM, van Strijp JAG, Croes M (2020) Combating Implant Infections: Shifting Focus from Bacteria to Host. *Adv Mater* 32(43):e2002962. <https://doi.org/10.1002/adma.202002962>
- Cuthrell KM, Tzenios N, Umber J (2022) Burden of Autoimmune Disorders. A Review *Asian J Immunol* 6(3):1–3
- Edache EI, Uzairu A, Mamza PA, Shallangwa GA, Azam M, Min K (2023) Methimazole and propylthiouracil design as a drug for anti-graves' disease: structural studies, Hirshfeld surface analysis, DFT calculations, molecular docking, molecular dynamics simulations, and design as a drug for anti-graves' disease. *J Mol Struct* 1289:135913. <https://doi.org/10.1016/j.molstruc.2023.135913>
- Diana T, Olivo PD, Kahaly GJ (2018) Thyrotropin Receptor Blocking Antibodies. *Horm Metab Res* 50(12):853–862. <https://doi.org/10.1055/a-0723-9023.PMID30286485>
- Chen CR, Hubbard PA, Salazar LM, McLachlan SM, Murali R, Rapoport B (2015) Crystal structure of a TSH receptor monoclonal antibody: insight into Graves' disease pathogenesis. *Mol Endocrinol* 29(1):99–107. <https://doi.org/10.1210/me.2014-1257>
- Nabi M, Noor R, Zahid A, Zulfiqar T, Khalid A, Riaz S (2022) Grave's Disease: Pathophysiology of a Model Autoimmune Disease. *Arch Microbiol Immunol* 6:149–164. <https://doi.org/10.26502/ami.93650083>
- Smith TJ, Hegedüs L (2016) Graves' Disease. *N Engl J Med* 375(16):1552–1565. <https://doi.org/10.1056/NEJMra1510030>
- Rice SA, Peden NR, McGlynn S, Morton C (2010) Atypical presentation of infiltrative thyroid dermatopathy. *Clin Exp Dermatol* 35(1):56–58. <https://doi.org/10.1111/j.1365-2230.2008.03109.x>
- Radziszewski M, Kuś A, Bednarczuk T (2023) Genotype-phenotype correlations in Graves' disease. *Best Pract Res Clin Endocrinol Metab* 37(2):101745. <https://doi.org/10.1016/j.beem.2023.101745>
- Kahaly GJ, Bartalena L, Hegedüs L, Leenhardt L, Poppe K, Pearce SH (2018) European Thyroid Association Guideline for the Management of Graves' Hyperthyroidism. *Eur Thyroid J* 7(4):167–186. <https://doi.org/10.1159/000490384>
- Poli D, Antonucci E (2015) Epidemiology, diagnosis, and management of atrial fibrillation in women. *Int J of women's health*, 605–614.
- Rago T, Cantisani V, Ianni F, Chiovato L, Garberoglio R, Durante C, Frasoldati A, Spiezia S, Farina R, Vallone G, Pontecorvi A (2018) Thyroid ultrasonography reporting: consensus of Italian Thyroid Association (AIT), Italian Society of Endocrinology (SIE), Italian Society of Ultrasonography in Medicine and Biology (SIUMB) and Ultrasound Chapter of Italian Society of Medical Radiology (SIRM). *J Endocrinol Invest* 41(12):1435–1443. <https://doi.org/10.1007/s40618-018-0935-8>
- Chaplin DD (2010) Overview of the immune response. *J Allergy Clin Immunol*. 125(2);Suppl 2:S3–23. doi: <https://doi.org/10.1016/j.jaci.2009.12.980>.
- Beutler B (2004) Inferences, questions and possibilities in Toll-like receptor signalling. *Nature* 430(6996):257–263. <https://doi.org/10.1038/nature02761>
- Hussain YS, Hookham JC, Allahabadia A, Balasubramanian SP (2017) Epidemiology, management and outcomes of Graves' disease-real life data. *Endocrine* 56(3):568–578. <https://doi.org/10.1007/s12020-017-1306-5>
- Nickoloff, B. J., & Nestle, F. O. (Eds.). (2008). *Dermatologic immunity*. Karger Medical and Scientific Publishers. 10: 344–58.
- AL-smadi K, Imran M, Leite-Silva VR, Mohammed Y, (2023) Vitiligo: A Review of Aetiology, Pathogenesis, Treatment, and Psychosocial Impact. *Cosmetics* 10(3):84
- Antonelli A, Ferrari SM, Ragusa F, Elia G, Paparo SR, Ruffilli I, Patrizio A, Giusti C, Gonnella D, Cristaudo A (2020) Foddiss R (2020) Graves' disease: Epidemiology, genetic and environmental risk factors and viruses. *Best Pract Res Clin Endocrinol Metab* 34(1):101387. <https://doi.org/10.1016/j.beem.2020.101387>
- Khan MS, Lone SS, Faiz S, Farooq I, Majid S (2021) Graves' Disease: Pathophysiology, Genetics and Management. *Graves' Disease*, p.67. doi: <https://doi.org/10.5772/intechopen.98238>.
- Zhou T, Huang D, Cafilisch A (2010) Quantum mechanical methods for drug design. *Curr Top Med Chem* 10(1):33–45. <https://doi.org/10.2174/156802610790232242>
- Adekoya OC, Adekoya GJ, Sadiku ER, Hamam Y, Ray SS (2022) Application of DFT Calculations in Designing Polymer-Based Drug Delivery Systems: an Overview. *Pharmaceutics* 14(9):1972. <https://doi.org/10.3390/pharmaceutics14091972>

24. Edache EI, Uzairu A, Mamza PA, Shallangwa GA (2022) Structure-based simulated scanning of rheumatoid arthritis inhibitors: 2D-QSAR, 3D-QSAR, docking, molecular dynamics simulation, and lipophilicity indices calculation. *Sci Afr* 15:e01088. <https://doi.org/10.1016/j.sciaf.2021.e01088>
25. Ugbe FA, Shallangwa GA, Uzairu A, Abdulkadir I (2021) Activity modeling, molecular docking and pharmacokinetic studies of some boron-pleuromutins as anti-wolbachia agents with potential for treatment of filarial diseases. *Chem Data Coll* 36:100783. <https://doi.org/10.1016/j.cdc.2021.100783>
26. Frisch MJ, Trucks GW, Schlegel HB, Scuseria GE, Robb MA, Cheeseman JR et al (2013) Gaussian;09, Revision D.01. Gaussian, Inc., Wallingford
27. Jastróž MH (2013) Vibrational energy distribution analysis (VEDA): scopes and limitations. *Spectrochim Acta A Mol Biomol Spectrosc* 114:220–230. <https://doi.org/10.1016/j.saa.2013.05.096>
28. Sanner MF (1999) Python: a programming language for software integration and development. *J Mol Graph Modell* 17:57–61
29. Valdés-Tresanco MS, Valdés-Tresanco ME, Valiente PA, Moreno E (2020) AMDock: a versatile graphical tool for assisting molecular docking with Autodock Vina and Autodock4. *Biol Direct* 15(1):12. <https://doi.org/10.1186/s13062-020-00267-2>
30. Trott O, Olson O (2010) AutoDock Vina: improving the speed and accuracy of docking with a new scoring function, efficient optimization, and multithreading. *J Comput Chem* 31(2):455–461. <https://doi.org/10.1002/jcc.21334>
31. Phillips JC, Braun R, Wang W, Gumbart J, Tajkhorshid E, Villa E, Chipot C, Skeel RD, Kale L, Schulten K (2005) Scalable molecular dynamics with NAMD. *J Comp Chem* 26(16):1781–1802. <https://doi.org/10.1002/jcc.20289>
32. Huang J, Rauscher S, Nawrocki G, Ran T, Feig M, de Groot BL, Grubmüller H, MacKerell AD Jr (2017) CHARMM36m: an improved force field for folded and intrinsically disordered proteins. *Nat Methods* 14(1):71–73. <https://doi.org/10.1038/nmeth.4067>
33. Humphrey W, Dalke A, Schulten K (1996) VMD: visual molecular dynamics. *J Mol Graph* 14(1):33–38. [https://doi.org/10.1016/0263-7855\(96\)00018-5](https://doi.org/10.1016/0263-7855(96)00018-5)
34. Bai Q, Tan S, Xu T, Liu H, Huang J, Yao X (2020) MolAICal: a soft tool for 3D drug design of protein targets by artificial intelligence and classical algorithm. *Brief Bioinform* 00:1–12. <https://doi.org/10.1093/bib/bbaa161>
35. Pino-Rios R, Inostroza D, Cárdenas-Jirón G, Tiznado W (2019) Orbital-weighted dual descriptor for the study of local reactivity of systems with (quasi-) degenerate states. *J Phys Chem A* 123(49):10556–10562. <https://doi.org/10.1021/acs.jpca.9b07516>
36. Pino-Rios R, Yañez O, Inostroza D, Ruiz L, Cardenas C, Fuentealba P et al (2017) Proposal of a simple and effective local reactivity descriptor through a topological analysis of an orbital-weighted Fukui function. *J Comp Chem* 38(8):481–488. <https://doi.org/10.1002/jcc.24699>
37. Khan E, Shukla A, Srivastava A, Shweta S, Tandon P (2015) Molecular structure, spectral analysis and hydrogen bonding analysis of ampicillin trihydrate: a combined DFT and AIM approach. *New J Chem* 39(12):9800–9812. <https://doi.org/10.1039/C5NJ01779C>
38. O'Boyle NM, Tenderholt AL, Langner KM (2008) cclib: a library for package-independent computational chemistry algorithms. *J Comput Chem* 29(5):839–845. <https://doi.org/10.1002/jcc.20823>
39. Edache EI, Dawi HA, Ugbe FA (2023) 3D-QSAR, molecular docking, molecular dynamics simulations and structural studies of some selected inhibitors of the glycoprotein (GPC) of Lassa virus. *J Appl Organomet Chem* 3(3):224–244. <https://doi.org/10.22034/JAOC.2023.410946.1103>
40. Wémeau JL, Klein M, Sadoul JL, Briet C, Vélouydom-Céphise FL (2018) Graves' disease: Introduction, epidemiology, endogenous and environmental pathogenic factors. *Ann Endocrinol (Paris)* 79(6):599–607. <https://doi.org/10.1016/j.ando.2018.09.002>
41. Ghamri M, Harkati D, Saleh BA, Chikhaoui AR, Belaidi S (2018) Molecular structure, Nbo charges, vibrational assignments, homolumo and Fukui functions of pyrazino [2, 3-D] pyrimidine based on DFT calculations. *Der Pharma Chemica* 10(6):179–187
42. Adindu EA, Godfrey OC, Agwupuye EI, Ekpong BO, Agurokpon DC, Ogbodo SE, Benjamin I, Louis H (2023) Structural analysis, reactivity descriptors (HOMO-LUMO, ELF, NBO), effect of polar (DMSO, EtOH, H<sub>2</sub>O) solvation, and libido-enhancing potential of resveratrol by molecular docking. *Chem Phys Impact* 7:100296. <https://doi.org/10.1016/j.chphi.2023.100296>
43. Ugbe FA, Edache EI, Adeniji SE, Arthur DE, Ajala A, Adawara SN, Ejeh S, Ibrahim ZY (2024) Computational evaluation of the inhibitory potential of some urea, thiourea, and selenourea derivatives of diselenides against leishmaniasis: 2D-QSAR, pharmacokinetics, molecular docking, and molecular dynamics simulation. *J Mol Struct* 1302:137473. <https://doi.org/10.1016/j.molstruc.2023.137473>
44. Demircioğlu Z, Kaştaş AC, Büyükgüngör O (2014) The spectroscopic (FT-IR, UV-Vis), Fukui function, NLO, NBO, NPA and tautomerism effect analysis of (*E*)-2-[(2-hydroxy-6-methoxybenzylidene) amino] benzonitrile. *Spectrochim Acta A Mol Biomol Spectrosc*. <https://doi.org/10.1016/j.saa.2014.11.078>
45. Damous M, Allal H, Belhocine Y, Maza S, Merazig H (2021) Quantum chemical exploration on the inhibition performance of indole and some of its derivatives against copper corrosion. *J Mol Liq* 340:117136. <https://doi.org/10.1016/j.molliq.2021.117136>
46. Ntieche Z, Abe MTO, Freidy OMG, Ejeh GW, Ndjaka JMB (2022) Electronic, non-linear optical, optoelectronic, and thermodynamic properties of undoped and doped bis (ethylenedithio) tetraselenafulvalene (BETS) (C<sub>10</sub>H<sub>8</sub>S<sub>4</sub>Se<sub>4</sub>) molecule: first study using ab initio investigation. *J Mol Model* 28(9):256. <https://doi.org/10.1007/s00894-022-05250-4>
47. Zhao Y, Truhlar DG (2006) A new local density functional for main-group thermochemistry, transition metal bonding, thermochemical kinetics, and noncovalent interactions. *J Chem Phys* 125(19):194101. <https://doi.org/10.1063/1.2370993>
48. Ferdous J, Kawsar SMA (2020) Thermochemical, molecular docking and ADMET studies of some methyl  $\alpha$ -D-glucopyranoside derivatives. *Chittagong Univ J Sci* 42(1):58–83. <https://doi.org/10.3329/cujvs.v42i1.54238>
49. Bouachrine M, Azaid A, Abram T, Kacimi R, Raftani M, Abdelouahid SBAÏ, Lakhliif T (2021) DFT/TDDFT studies of the structural, electronic, NBO and non-linear optical properties of triphenylamine functionalized tetrathiafulvalene. *Theor Chem* 5(2):24–34
50. Ebenso EE, Kabanda MM, Arslan T, Saracoglu M, Kandemirli F, Murulana LC, Singh AK, Shukla SK, Hammouti B, Khaled KF, Quraishi MA (2012) Quantum chemical investigations on quinoline derivatives as effective corrosion inhibitors for mild steel in acidic medium. *Int J Electrochem Sci* 7(6):5643–5676. [https://doi.org/10.1016/S1452-3981\(23\)19650-7](https://doi.org/10.1016/S1452-3981(23)19650-7)
51. Lu T, Chen Q (2021) Shermo: a general code for calculating molecular thermochemistry properties. *Comput Theor Chem* 1200:113249. <https://doi.org/10.1016/j.comptc.2021.113249>
52. Jeyavijayan S (2015) Molecular structure, vibrational spectra, NBO analysis, first hyperpolarizability, and HOMO–LUMO studies of 2-amino-4-hydroxypyrimidine by density functional method. *J Mol Struct* 1085:137–146. <https://doi.org/10.1016/j.molstruc.2014.12.047>
53. Abe MO, Nzia CL, Sidjui LS, Kamsi RY, Mveme CDD, Assatse YT, Ndjaka JMB, Ejeh GW (2021) Predictive calculation of structural, nonlinear optical, electronic and thermodynamic properties

- of andirobin molecule from ab initio and DFT methods. *SN Appl Sci* 3(9):768. <https://doi.org/10.1007/s42452-021-04749-4>
54. Bee S, Agarwal P, Gupta A, Tandon P (2013) Use of vibrational spectroscopy to study 2-[4-(*N*-dodecanoylamino)phenyl]-5-(4-nitrophenyl)-1,3,4-oxadiazole: a combined theoretical and experimental approach. *Spectrochim Acta A Mol Biomol Spectrosc* 114:236–255. <https://doi.org/10.1016/j.saa.2013.05.051>
55. Thamarai A, Vadamar R, Raja M, Muthu S, Narayana B, Ramesh P, Muhamed RR, Sevvanthi S, Aayisha S (2020) Molecular structure interpretation, spectroscopic (FT-IR, FT-Raman), electronic solvation (UV-Vis, HOMO-LUMO and NLO) properties and biological evaluation of (2*E*)-3-(biphenyl-4-yl)-1-(4-bromophenyl) prop-2-en-1-one: experimental and computational modeling approach. *Spectrochim Acta A Mol Biomol Spectrosc* 226:117609. <https://doi.org/10.1016/j.saa.2019.117609>
56. Sevvanthi S, Muthu S, Raja M, Aayisha S, Janani S (2020) PES, molecular structure, spectroscopic (FT-IR, FT-Raman), electronic (UV-Vis, HOMO-LUMO), quantum chemical and biological (docking) studies on a potent membrane permeable inhibitor: dibenzoxepine derivative. *Heliyon* 6(8):e04724. <https://doi.org/10.1016/j.heliyon.2020.e04724>
57. Edache EI, Uzairu A, Mamza PA, Shallangwa GA, Ibrahim MT (2023) Towards designing of some potential new autoimmune disorder inhibitors using crystal structures and Hirshfeld surface analyses in combination with molecular docking and molecular dynamics simulations. *Intell Pharm*. <https://doi.org/10.1016/j.ijpha.2023.11.008>
58. George J, Prasana JC, Muthu S, Kuruvilla TK, Sevvanthi S, Saji RS (2018) Spectroscopic (FT-IR, FT Raman) and quantum mechanical study on *N*-(2, 6-dimethylphenyl)-2-[4-[2-hydroxy-3-(2-methoxyphenoxy) propyl] piperazin-1-yl] acetamide. *J Mol Struct* 1171:268–278. <https://doi.org/10.1016/j.molstruc.2018.05.106>
59. Muthu S, Ramachandran G (2014) Spectroscopic studies (FTIR, FT-Raman and UV-visible), normal coordinate analysis, NBO analysis, first order hyper polarizability, HOMO and LUMO analysis of (1*R*)-*N*-(prop-2-yn-1-yl)-2, 3-dihydro-1*H*-inden-1-amine molecule by ab initio HF and density functional methods. *Spectrochim Acta A Mol Biomol Spectrosc* 121:394–403. <https://doi.org/10.1016/j.saa.2013.10.093>
60. Bharathy G, Prasana JC, Muthu S, Irfan A, Asif FB, Saral A, Aayisha S (2021) Evaluation of electronic and biological interactions between *N*-[4-(ethylsulfamoyl) phenyl] acetamide and some polar liquids (IEFPCM solvation model) with Fukui function and molecular docking analysis. *J Mol Liq* 340:117271. <https://doi.org/10.1016/j.molliq.2021.117271>
61. Ugbe FA, Shallangwa GA, Uzairu A, Abdulkadir I (2022) Theoretical modeling and design of some pyrazolopyrimidine derivatives as Wolbachia inhibitors, targeting lymphatic filariasis and onchocerciasis. *In Silico Pharmacol* 10(1):8. <https://doi.org/10.1007/s40203-022-00123-3>
62. Ochu SR, Edache EI, Shafiu S, Idowu AE (2017) Docking studies of a series of fluphenazine as potential IRE1 (X-ray crystal structure of caspase-3) inhibitors: a rational approach to anticancer drug design. *J Adv Chem Sci* 3(3):494–495
63. Edache EI, Uzairu A, Mamza PA, Shallangwa GA (2022) Theoretical investigation of the cooperation of iminoguanidine with the enzymes-binding domain of Covid-19 and bacterial lysozyme inhibitors and their pharmacokinetic properties. *J Mex Chem Soc* 66(4):513–542. <https://doi.org/10.29356/jmcs.v66i4.1726>
64. Edache EI, Uzairu A, Mamza PA, Shallangwa GA (2020) Prediction of HemO inhibitors based on iminoguanidine using QSAR, 3DQSAR study, molecular docking, molecular dynamic simulation and ADMET. *Drug J Design Discov Res* 1(2):36–52
65. Reynolds CH, Bembenek SD, Toungue BA (2007) The role of molecular size in ligand efficiency. *Bioorg Med Chem Lett* 17(15):4258–4261. <https://doi.org/10.1016/j.bmcl.2007.05.038>
66. Keserü GM (2009) The influence of lead discovery strategies on the properties of drug candidates. *Nat Rev Drug Discov* 8(3):203–212. <https://doi.org/10.1038/nrd2796>, PMID19247303
67. Edache EI, Uzairu A, Mamza PA, Shallangwa GA (2021) Docking simulations and virtual screening to find novel ligands for T3S in *Yersinia pseudotuberculosis* YPIII, A drug target for type III secretion (T3S) in the Gram-negative pathogen *Yersinia pseudotuberculosis*. *Chem Rev Lett* 4:130–144. <https://doi.org/10.22034/CRL.2021.254804.1088>
68. Zhao YH, Abraham MH, Le J, Hersey A, Luscombe CN, Beck G, Sherborne B, Cooper I (2002) Rate-limited steps of human oral absorption and QSAR studies. *Pharm Res* 19(10):1446–1457. <https://doi.org/10.1023/a:1020444330011>

**Publisher's Note** Springer Nature remains neutral with regard to jurisdictional claims in published maps and institutional affiliations.